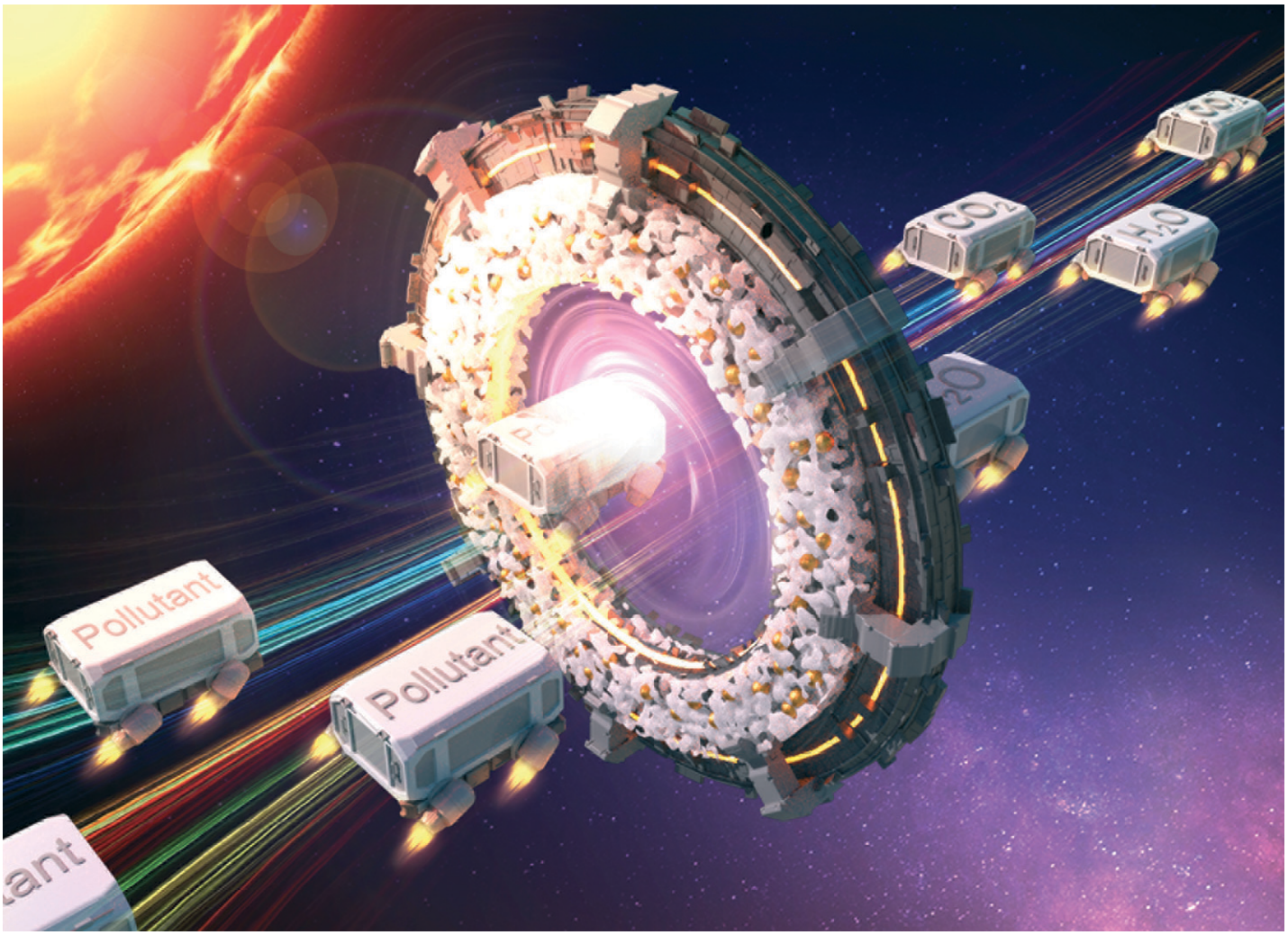

Showcasing research from Xinghui Liu's laboratory, Hubei Institute of Aerospace Chemotechnology, Xiangyang, China.

Enhanced pollutant photodegradation activity of graphitic carbon nitride on *via* bismuth oxyhalide graphene hybridization and the mechanism study

The Z-scheme heterojunction structure of g-C_3N_4 and $Bi_4O_5Br_2$ adjusts the band positions of the dominant active species, providing suitable energy levels for the generation of h^+ and $\cdot O_2^-$, enhanced pollutant degradation.

Image reproduced by permission of Xinghui Liu and Fuchun Zhang from *Ind. Chem. Mater.*, 2025, **3**, 191.

As featured in:

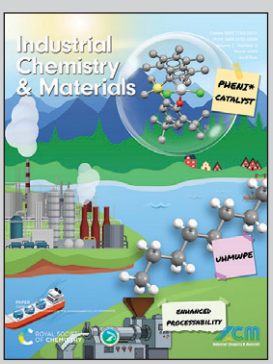

See Xinghui Liu, Xiang Guo, Fuchun Zhang, Yongfa Zhu *et al.*, *Ind. Chem. Mater.*, 2025, **3**, 191.

ROYAL SOCIETY OF CHEMISTRY

Industrial Chemistry & Materials

Industrial Chemistry & Materials

ROYAL SOCIETY OF CHEMISTRY

PAPER

View Article Online
View Journal | View Issue

Cite this: *Ind. Chem. Mater.*, 2025, **3**, 191

Enhanced pollutant photodegradation activity of graphitic carbon nitride on *via* bismuth oxyhalide graphene hybridization and the mechanism study†

Xinghui Liu, ‡*[ab] Yang Liu,‡[ab] Xiang Guo,*[b] Bowen Tao,[b] Xu Ma,[a] Simin Cheng,[a] Ning Tian,[a] Gaihui Liu,[a] Qiao Wu,[a] Viet Q. Bui,[c] Kuldeep K. Saxena,[d] Sankar Ganesh Ramaraj,[e] Jianhui Liu,[f] Fuchun Zhang*[a] and Yongfa Zhu*[g]

Addressing the degradation of persistent organic pollutants like bisphenol A (BPA) and rhodamine B (RhB) with a photocatalyst that is both cost-effective and environmentally friendly is a notable challenge. This research presents the synthesis of an optimized g-C_3N_4/$Bi_4O_5Br_2$ composite featuring a Z-scheme heterojunction structure. The precise band alignment of this composite significantly enhances the separation of photogenerated charges and the production of dominant reactive species. The composite demonstrated exceptional photocatalytic performance, with BPA degradation efficiency nearing 98% and RhB achieving complete degradation within 80 and 35 min under visible light, respectively. These results are approximately 1.3 times greater than the individual performance of CN and BOB, surpassing recent literature benchmarks. Through EPR and free radical capture experiments, the role of h^+ and $\cdot O_2^-$ as the primary active free radicals in the degradation process have been confirmed. First-principles calculations validated the experimental results, indicating that the Z-type heterojunction is instrumental in generating active species, thus improving degradation efficiency. This study offers a promising strategy for the design of photocatalysts targeting emerging organic pollutants.

Received 20th August 2024,
Accepted 23rd September 2024

DOI: 10.1039/d4im00105b

rsc.li/icm

Keywords: Photocatalysis; g-C_3N_4; $Bi_4O_5Br_2$; Heterostructure; Water purification; Z-scheme.

1 Introduction

Resource depletion and environmental pollution are major challenges facing society today, and there is an urgent need to develop environmentally friendly, cost-effective and efficient technologies for the treatment of difficult-to-degrade organic wastewater to promote sustainable development.[1] Advanced oxidation processes, including biochar,[2] chemicals,[3] photocatalytic,[4] electrical[5] and photoelectrochemical[6] oxidation processes, are gaining attention for efficient water treatment.[7]

In 1972, Fujishima and Honda set an important milestone in the field of photocatalysis by using n-type titanium dioxide and platinum electrodes for water decomposition,[8] which has since expanded to include dye degradations using many myriad semiconductor materials such as α-Fe_2O_3,[9] WO_3,[10] ZnO,[11] layered double hydroxides (LDHs),[12] and g-C_3N_4.[13–15] MOFs (metal–organic frameworks) and COFs (covalent organic frameworks) show great potential in photocatalysis.[16,17] And single catalysts are limited in photocatalytic applications mainly due to the problems of wide bandgap, low solar energy conversion efficiency, easy corrosion, easy aggregation, and rapid complexation of electron–hole pairs.

To enhance the light utilization and effectively separate the photoinduced electron–hole pair, heteroatom doping,[18] metal loading,[19] and constructed heterojunction[16,20,21] strategies were adopted. Designing heterojunctions is the most promising approach to minimize the recombination of electron–hole pairs

[a] *School of Physics and Electronic Information, Yan'an University, Yan'an 716000, China. E-mail: liuxinghui119@gmail.com, yadxzfc@yau.edu.cn*
[b] *Science and Technology on Aerospace Chemical Power Laboratory, Laboratory of Emergency Safety and Rescue Technology, Hubei Institute of Aerospace Chemotechnology, Xiangyang, 441003, China. E-mail: guoxiang@casc42.cn*
[c] *Advanced Institute of Science and Technology, The University of Danang, 41 Le Duan, Danang, Vietnam*
[d] *Division of Research and Development, Lovely Professional University, Phagwara, India*
[e] *Department of Bioengineering, The University of Tokyo, 7-3-1 Hongo, Bunkyo-Ku, Tokyo, 113-8656, Japan*
[f] *Department of Restorative Dentistry and Biomaterials Sciences, Harvard School of Dental Medicine Boston, Massachusetts United States of America, The Forsyth Institute Cambridge, Massachusetts, USA*
[g] *Department of Chemistry, Beijing Key Laboratory for Analytical Methods and Instrumentation, Tsinghua University, Beijing 100084, China. E-mail: zhuyf@tsinghua.edu.cn*

† Electronic supplementary information (ESI) available. See DOI: https://doi.org/10.1039/d4im00105b

‡ These authors contributed equally to this work.

while maximizing pollutants degradation efficiency. Bismuth oxyhalide photocatalysts, classified as ternary (V–VI–VII) semiconductors with the formula BiOX (X = Cl, Br, I), possess a distinctive two-dimensional (2D) layered structure and broad light-responsive capabilities owing to their suitable bandgap. This characteristic has garnered significant attention to control photocatalytic environments and energy conversion processes.[22,23] The accepted notion is that the bandgap value of BiOX becomes small (X = Cl, ~3.2 eV; X = Br, ~2.7 eV; X = I, ~1.7 eV) along with the increasing atomic number.[24] BiOBr has garnered considerable attention due to its favorable bandgap value compared to other BiOX materials.[24,25] Liu *et al.* pass and Li *et al.* significantly improved the separation and transfer efficiency of photogenerated electron–hole pairs and the redox capacity through the strategies of doping and building heterostructures, respectively.[26,27] $Bi_4O_5Br_2$ (BOB), a representative type of BiOBr, has exhibited excellent performance in the photocatalytic degradation of organically polluted wastewater because of its high chemical stability and non-toxic, pollution-free circulation stability.[28–31]

Recently, g-C_3N_4 (CN), an intriguing, conjugated 2D material with tertiary amine fragments, has drawn multidisciplinary attention as a potential co-catalyst in visible light photocatalysis with excellent thermal and chemical stability.[15,32] Previous studies on g-C_3N_4/$Bi_4O_5Br_2$ (CN/BOB), such as Zhou *et al.*, explored the effects of catalyst preparation conditions (*e.g.*, g-C_3N_4 content, pH, hydrothermal reaction temperature, and time) on the degradation.[33] In contrast, Yi *et al.* used a precipitation method to prepare BOB/CN with a 2D/2D nanosheet structure for the first time, significantly improving its adsorption and photocatalytic abilities.[34] Zhao *et al.* successfully prepared BOB/CN heterostructures using a facile water-induced self-assembly method, which can promote carrier transfer and provide vital redox electrons to reduce $\cdot O_2^-$ and holes to oxidize water.[35] Li *et al.* established a facile microwave-assisted strategy to synthesize photocatalysts, which, under blue LED irradiation, can significantly improve benzyl alcohol conversion efficiency and high selectivity.[36]

Herein, we constructed CN/BOB heterojunction *via* a simple hydrothermal and heat-treating post-process. Various mass ratio CN/BOB heterostructures were fabricated, and optimized CN/BOB-16 catalysts were systematically studied using experimental and theoretical tools. Notably, under visible light conditions, the degradation rate of bisphenol A (BPA) and rhodamine B (RhB) dyes surpasses that of comparable catalysts.[37,38] We have deeply explored the photocatalytic degradation pathway of bisphenol A (BPA) by high performance liquid chromatography-mass spectrometry (HPLC-MS), which not only verified the effectiveness of CN/BOB composites in the degradation of BPA, but also revealed more intermediates and degradation pathways, which provided more detailed insights into understanding the performance of the materials in the photocatalytic process. In addition, we proposed a Z-scheme electron transfer mechanism by density-functional theory (DFT) calculations and accurately determined the figure of merit and surface electronic structure by combining *in situ* X-ray photoelectron spectroscopy (*in situ* XPS) and ultraviolet photoelectron spectroscopy (UPS) experiments, which provided strong experimental evidence for the energy band arrangement. We have also utilized a variety of spectroscopic and electrochemical techniques, such as surface photovoltage spectroscopy, transient fluorescence spectroscopy, fluorescence lifetime spectroscopy, electrochemical impedance spectroscopy, and transient photocurrent testing, to further confirm the advantages of Z-scheme heterojunctions in reducing electron–hole complexation and increasing carrier lifetime. Our studies were not limited to the degradation of a single pollutant, but extended to a wide range of pollutants, including phenolic compounds and a variety of dyes, demonstrating the broad applicability and great potential of our catalysts for treating a wide range of real pollutants. Through the above combined experimental and theoretical evaluations, we have gained a deeper understanding of the performance of CN/BOB photocatalytic degradation materials, which provides a broader basis for future research on this type of heterojunction materials.

2 Results and discussion

2.1 Construction and confirmation of heterojunctions

2.1.1 Preparation and structural characterization of g-C_3N_4/$Bi_4O_5Br_2$. The synthesis procedure of CN/BOB heterostructure and BPA(RhB) degradation is schematically illustrated in Fig. 1. BOB was synthesized *via* a straightforward hydrothermal method at 180 °C, while CN was prepared using thermal polycondensation at 550 °C (Fig. S2†). The CN/BOB heterostructures were synthesized and optimized by controlling the mass ratios of CN and BOB, including 2 : 1, 1 : 1, 1 : 2, 1 : 4, 1 : 6, 1 : 8, and 1 : 10. Those catalysts were named CN/BOB-21, CN/BOB-11, CN/BOB-12, CN/BOB-14, CN/BOB-16, CN/BOB-18, CN/BOB-110, respectively. The crystal structures of CN/BOB were analyzed using X-ray diffraction (XRD) patterns (Fig. 2a and S3†), showing the successful fabrication of CN-BOB heterostructures that contain g-C_3N_4 (PDF#87-1526)[39] and $Bi_4O_5Br_2$ (PDF#37-0699).[40] Two characteristic peaks at 12.5° and 27.2° were associated with the (100) and (002) crystal planes of the CN. The peaks located at 24.1°, 29.3°, 31.7°, 42.9°, 45.5°and 55.2° were ascribed to the (112), (113), (020), (105), (422) and (811) crystal planes of cubic BOB. At low concentrations of CN, the XRD patterns closely resembled those of BOB, suggesting that the coupling between CN and BOB did not alter the crystal structure of BOB, thus facilitating the photocatalytic degradation process.[41]

The surface element composition was explored through XPS survey spectra (Fig. S4†), confirming the successful fabrication of CN/BOB due to containing C, N, O, Bi, and Br elements, consistent with the XRD pattern. The N 1s spectra (Fig. 2c) of CN/BOB-16 heterojunction show the sp^2-hybridized nitrogen of C–N=C at ~398.5, the tertiary nitrogen of N–$(C)_3$ at ~399.4, and the free amino group of C–N–H at ~400.7.[42] Note that N 1s in CN/BOB-16 has a lower energy shift than that in CN. Three peaks centered at ~284.8 eV, ~286.0 eV and ~288.0 eV was

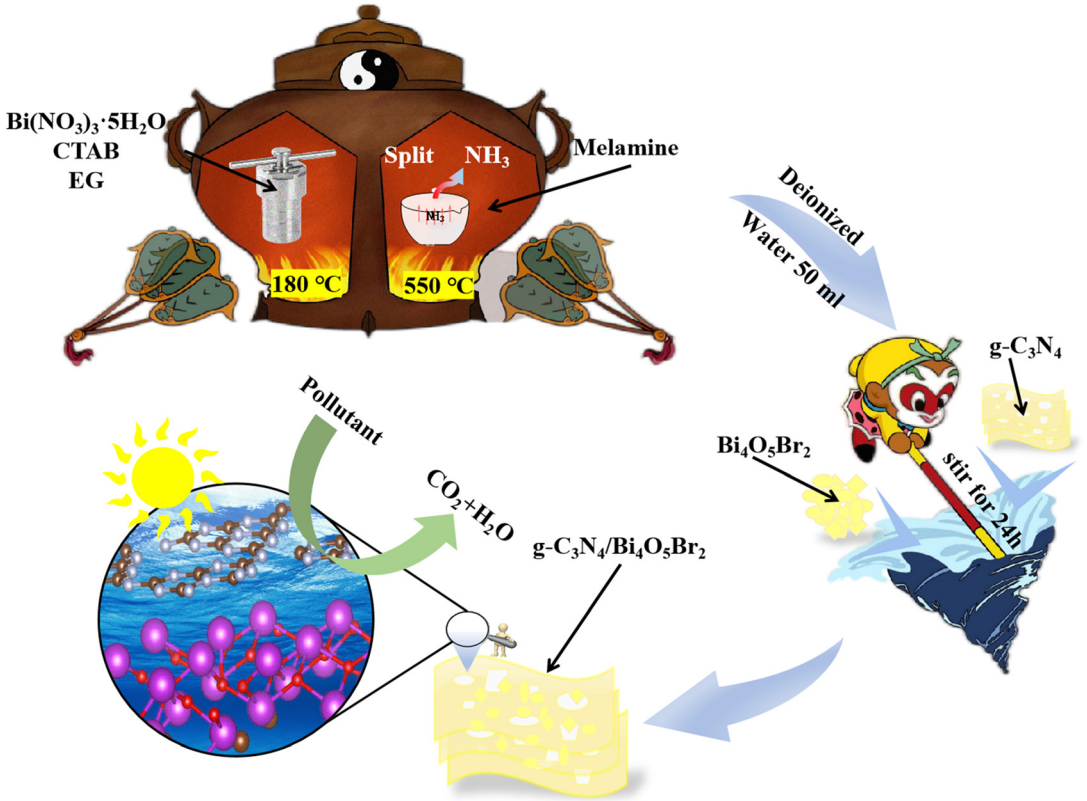

Fig. 1 The synthesis procedure demonstration: Schematic illustration of the preparation strategy of g-C_3N_4/$Bi_4O_5Br_2$-16. EG: ethylene glycol; CTAB: hexadecyl trimethyl ammonium bromide.

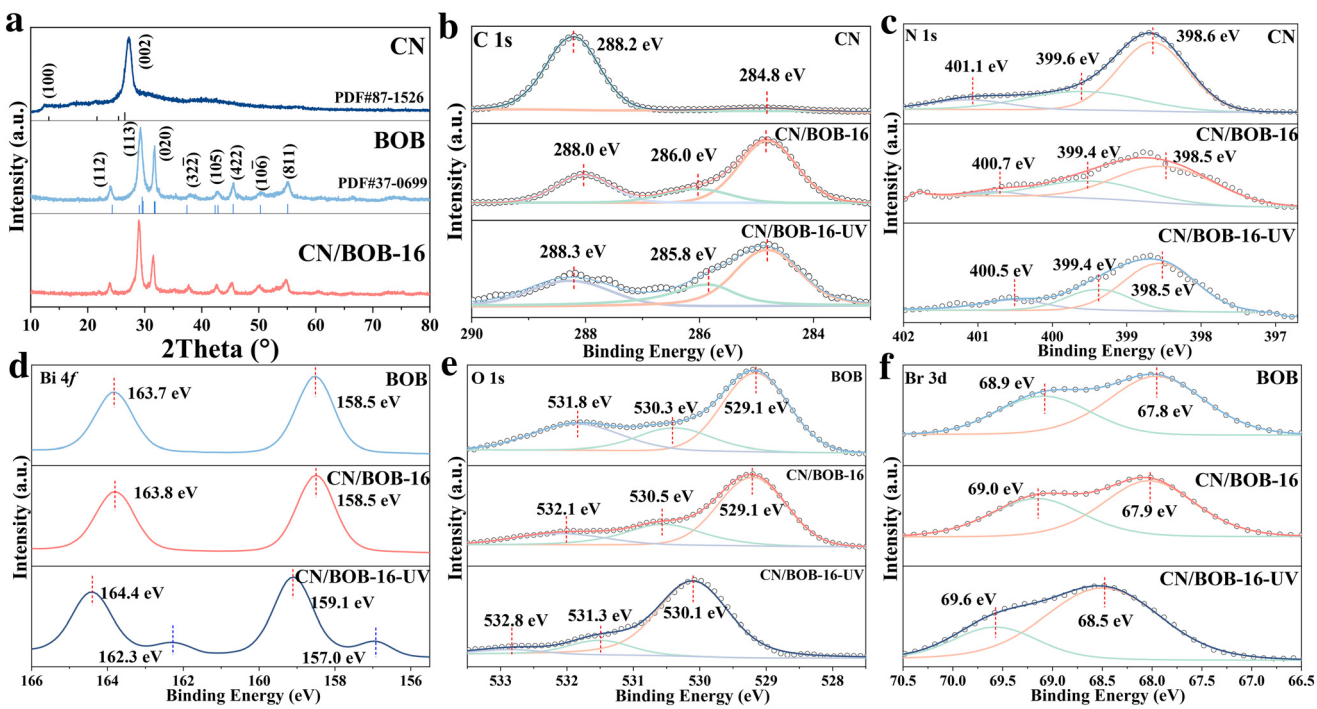

Fig. 2 Structure characterization: (a) XRD pattern; XPS spectra normal and *in situ* irradiated XPS of (b) C 1s, (c) N 1s, (d) Bi 4f, (e) O 1s and (f) Br 3d.

related with C–C bonds, C–N and N–C–N bonds, respectively. A similar phenomenon was observed for the peak of C 1s (Fig. 2b), indicating that CN obtained the electron from BOB. O 1s XPS spectra (Fig. 2e) show the three peaks attributed to the lattice oxygen (~529.1 eV), adsorbed hydroxide (~530.3 eV), and adsorbed water (~531.8 eV) for CN/BOB-16. The Bi 4f spectra (Fig. 2d) of CN/BOB-16 display two peaks at approximately ~158.52 eV (Bi $4f_{7/2}$) and 163.80 eV (Bi $4f_{5/2}$), indicating the presence of Bi^{3+}.[43] Br 3d spectra (Fig. 2f) of CN/BOB-16 has two peaks at 67.9 eV and 68.9 eV.[44]

The elemental chemical state of CN/BOB-16 exhibits a higher energy shift compared to that of pure BOB (Fig. 2d–f), suggesting that CN acquired electrons from BOB. This observation is consistent with the XPS data of C 1s and N 1s (Fig. 2c and b). The findings indicate that an internal electron field at the interface between CN and BOB facilitates electron transfer from BOB to CN, indicating a strong interaction between CN and BOB and confirming that CN/BOB was successfully constructed.

In situ irradiated XPS further verified the transfer pathway of photogenerated carriers. Compared to CN/BOB-16 in the dark, the binding energy of N 1s in CN/BOB-16-UV under UV irradiation shifted to a lower energy level (Fig. 2c). As shown in Fig. 2d–f, compared to the non-irradiated condition, the

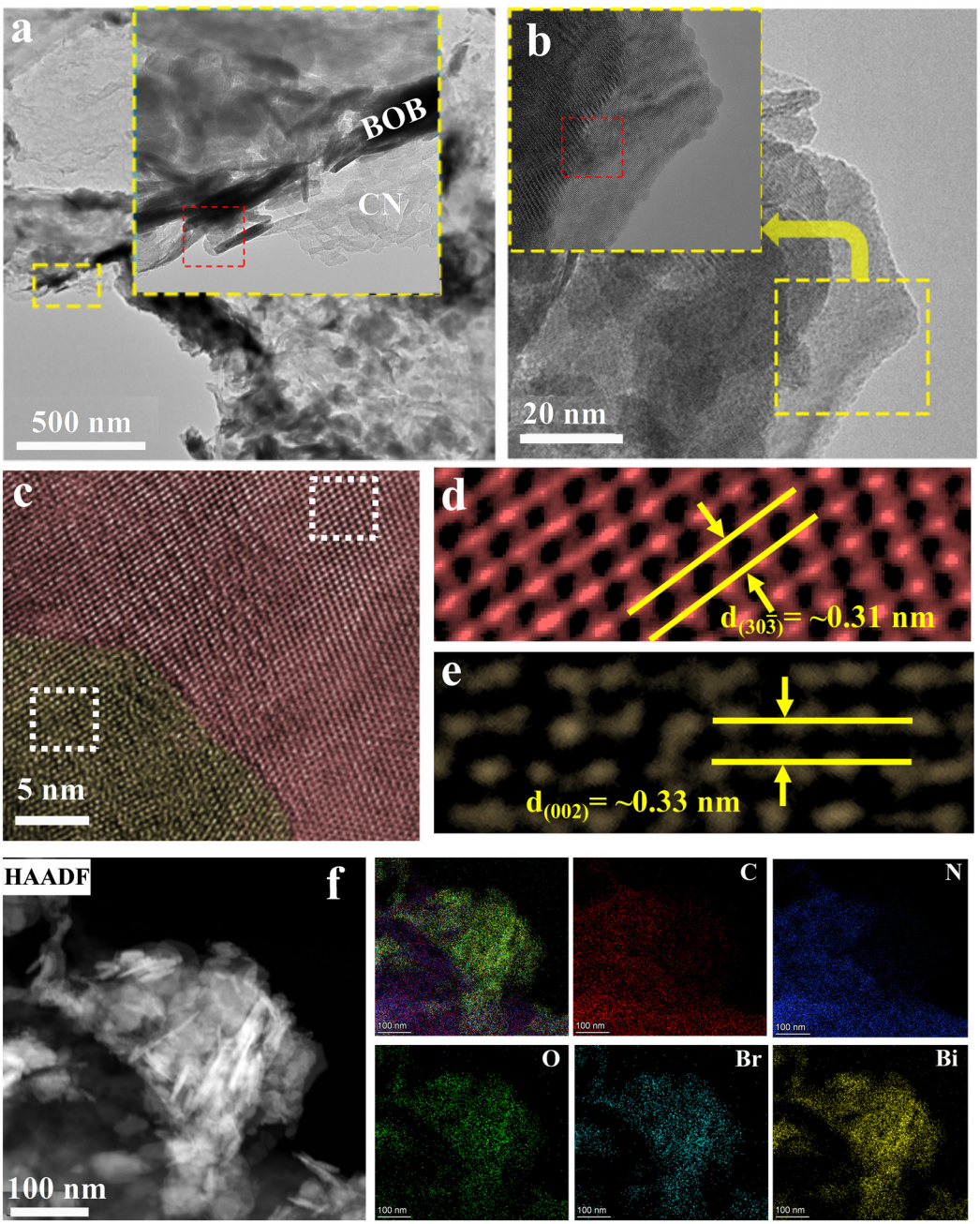

Fig. 3 Analysis morphology characterization of g-C_3N_4/$Bi_4O_5Br_2$ by TEM. (a–e) TEM images; (f) TEM-EDS elemental mapping images.

binding energies of Bi 4f, O 1s, and Br 3d in CN/BOB-16-UV exhibited significant positive shifts. This confirmed that the transfer pathway of photogenerated carriers is from BOB to CN. Additionally, a pair of sub-peaks with lower binding energies were observed in Bi 4f of CN/BOB-16-UV, which could be attributed to the reduced metallic Bi^0 after UV irradiation. Metallic bismuth can be introduced into bismuth compounds through photoreduction to enhance the reactivity of the catalytic system, effectively improving visible light absorption and promoting the separation of photogenerated carriers.[6]

2.1.2 Morphology characterization. Scanning electron microscopy (SEM) was conducted to assess the morphology of the prepared samples (Fig. S5†). As a result, pure BOB presented many micro and nanosheet clusters (Fig. S5a†), and pristine CN exhibited curved lamellar structures (Fig. S5b†). In Fig. S5c,† the small size of BOB particles is evident, coating the surface of CN and facilitating intimate interfacial contact between CN and BOB. This observation is further supported by transmission electron microscopy (TEM) images (Fig. 3a–e).

The insert image of Fig. 3a shows the two-part CN and BOB, evidenced by the EDS. Fig. 3f displays the presence of C, N, O, Bi, and Br elements, consistent with the XPS survey spectra, confirming the successful fabrication of the CN/BOB-16 heterojunction. HRTEM images of CN/BOB-16 (Fig. 3b–e) illustrate crystal facets measuring approximately 0.31 nm and 0.33 nm, corresponding to the $(30\bar{3})$ facet of BOB and the (002) facet of CN, respectively.

2.1.3 Confirmation of heterojunction type. To gain insight into the band scheme of the heterostructure of CN/BOB-16, it is essential to know the work function before/after contact between the CN and BOB. Density functional theory (DFT) calculations were conducted for the $(30\bar{3})$ facet of BOB, (002) facet of CN, and CN/BOB interface, work function of 2.98 eV,

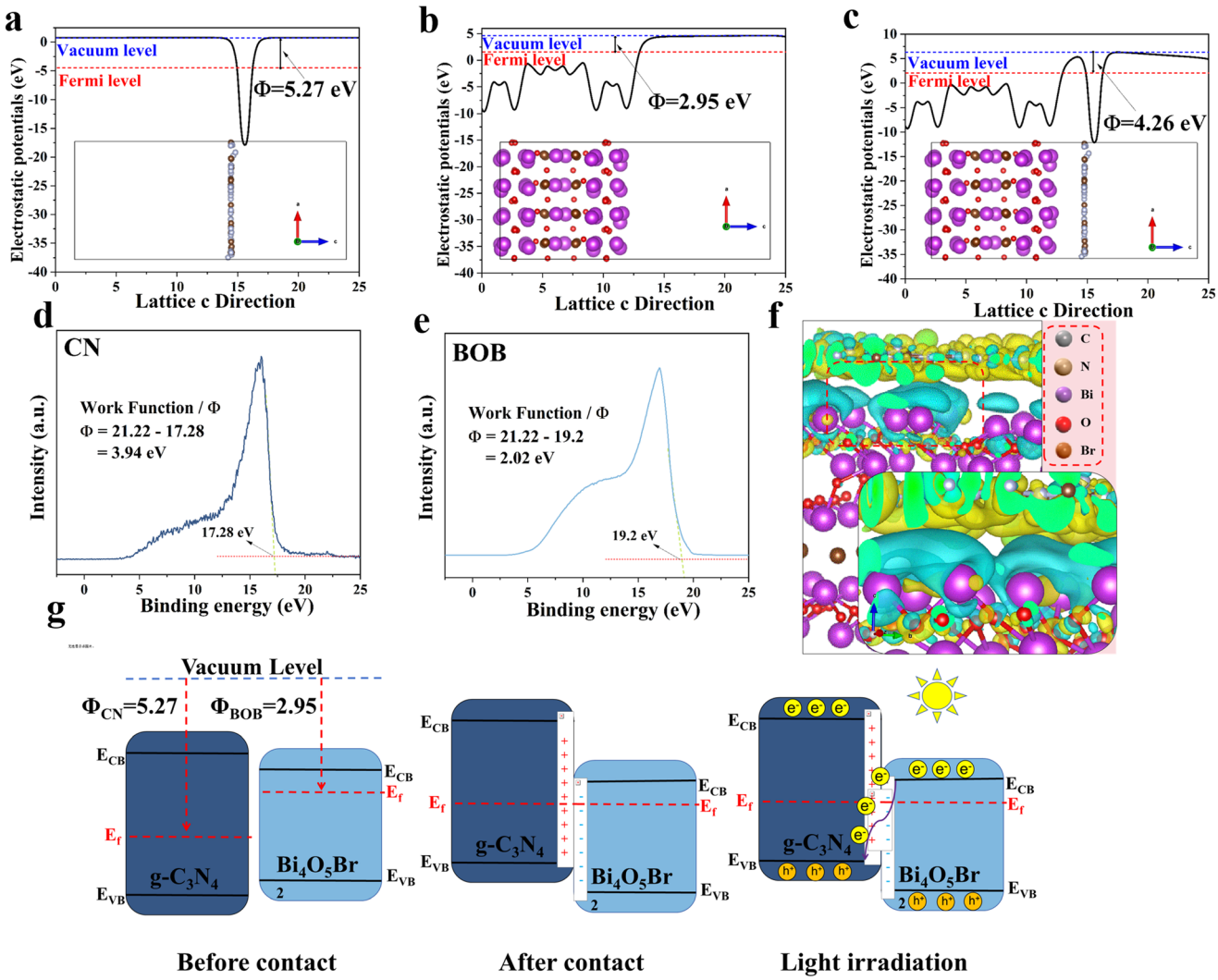

Fig. 4 (a–c) The calculated work function for $Bi_4O_5Br_2$ $(30\bar{3})$, g-C_3N_4 (002), and g-C_3N_4/$Bi_4O_5Br_2$. Red and blue dashed lines are the Fermi and vacuum levels; (d and e) UPS work function spectra of (a) g-C_3N_4 and (b) $Bi_4O_5Br_2$; (f) charge density difference for g-C_3N_4/$Bi_4O_5Br_2$ heterojunction. Yellow and cyan regions represent electron accumulation and depletion; (g) schematic diagram of carrier migration mechanism based on Z-scheme heterojunction.

5.09 eV, and 3.46 eV, respectively (Fig. 4a–c). We also conducted Mott–Schottky characterization tests on CN and BOB, and the results are shown in Fig. S6.† The slope of the Mott–Schottky curve is related to the type of semiconductor. When the slope is positive, the semiconductor is considered an n-type semiconductor. Since the Mott–Schottky curves of CN and BOB have positive slopes. Therefore, CN and BOB are n-type semiconductors, which is also consistent with the conclusion of Zhou *et al.* because the flat-band potential values of CN and BOB are −1.22 and −0.32 eV. The difference

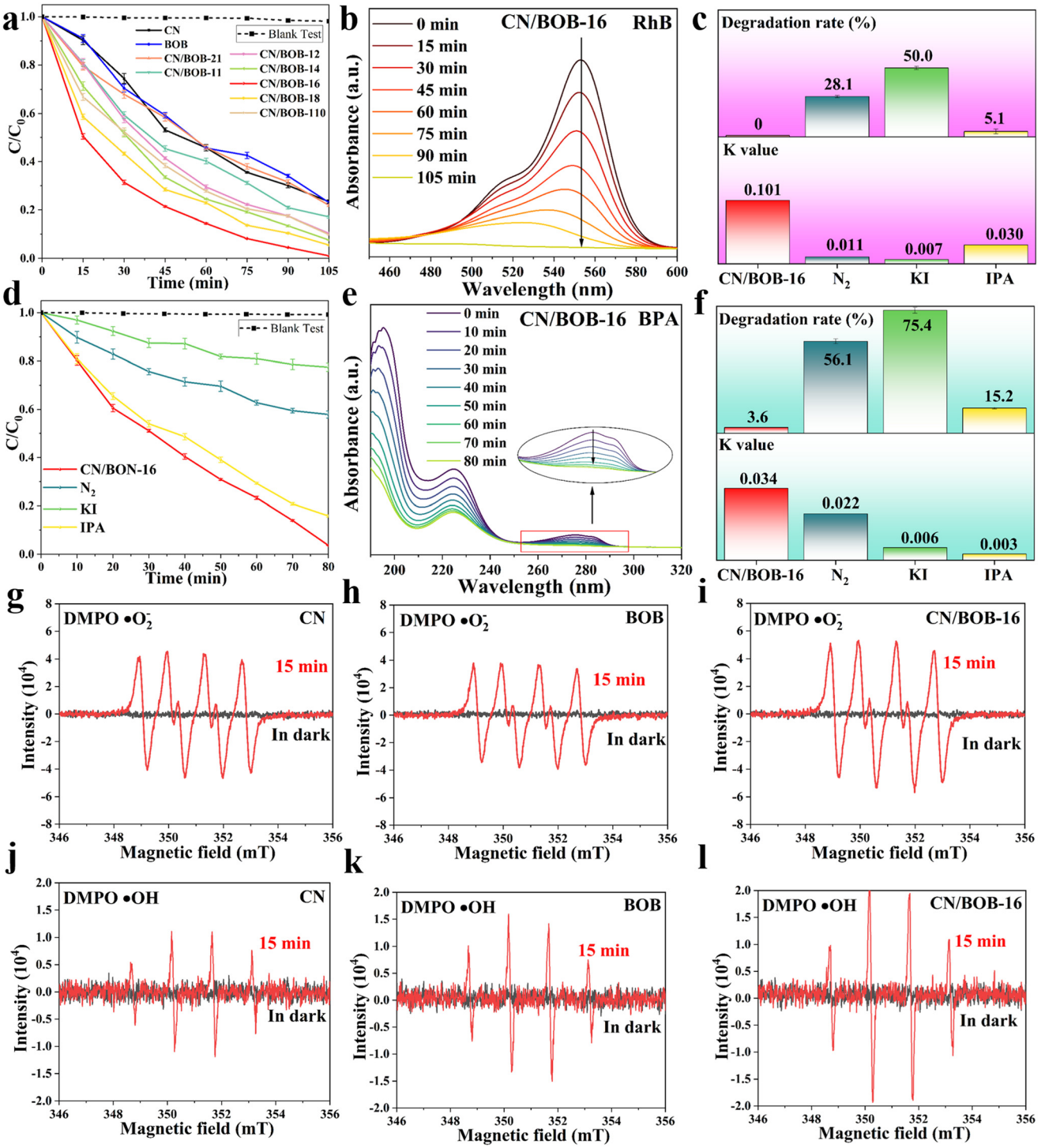

Fig. 5 Photocatalytic degradation performance evaluation using RhB & BPA. (a) RhB and (d) BPA concentration (C/C_0) against photodegradation time; UV-vis absorption spectroscopy of (b) RhB and (e) BPA solutions after the reaction of catalysts at different times; the slope of degradation rate and extent of degradation of CN/BOB-16 ((c) RhB and (f) BPA) before and after addition of capture agent; EPR signals of CN, BOB, and CN/BOB-16 for (g–i) DMPO-·O_2^- and (j–l) DMPO-·OH generated under visible light.

in potential of Ag/AgCl concerning the standard hydrogen electrode is 0.197 eV, so the conduction bands of CN and BOB are −1.06 eV and −0.13 eV, respectively. The UV-vis data of CN and BOB were analyzed using the Kubelka–Munk theorem, and the corresponding band gaps (E_g) were 2.60 eV and 2.16 eV (Fig. 6a and S7†), respectively. The valence band (VB) potentials of CN and BOB were calculated to be 1.54 and 2.03 V (*vs.* NHE), respectively.

To ensure that the heterojunction type is determined accurately, we obtained the work function (WF) of CN and BOB using ultraviolet photoelectron spectroscopy (UPS). As shown in Fig. 4d and e, the WF of CN and BOB are 3.94 and 2.02, respectively. The WF obtained by UPS is consistent with the trend of the results obtained from the DFT calculations. The results above demonstrate the band scheme before/after the contact between CN and BOB (Fig. 4g). It's worth noting that the band bending at the interface of the CN/BOB heterojunction inhibits the recombination of photoinduced electrons and holes generated at the valence band (VB) and conduction band (CB) positions in CN and BOB, respectively, which can be attributed to the build-in electrostatic potential field between the BOB and the CN. Additionally, charge density difference simulations were conducted using DFT, revealing electron transfer from BOB to CN attributed to the built-in electrostatic potential field (Fig. 4f). This finding aligns with the band scheme depicted in Fig. 4g and is supported by XPS results.

Based on the study's findings, the photoinduced carrier migration in CN/BOB can be described as a direct Z-scheme (Fig. 4g), facilitating the separation of photoinduced carriers and maximizing photodegradation efficiency. Photoinduced electrons in the BOB migrate to the CN until the Fermi level aligns. Consequently, the energy band edge in the CN, characterized by a high Fermi level, gradually bends upward towards the interface, while the energy band edge in the BOB, featuring a low Fermi level, bends downward. Consequently, electrons of BOB are combined with the hole CN, while holes of BOB and electrons of CN are confined to the VB and CB for the photodegradation reaction.[30]

2.2 Photocatalytic degradation characterization

We conducted the blank experiment with the same experimental condition to gain insight into the intrinsic catalysts and eliminate the light effect, demonstrating the negligible self-photolysis for the RhB and BPA (Fig. S8†). When as-prepared photocatalysts were adopted, the BPA/RhB concentration progressively decreased with irradiation time (Fig. 5a and d). As the CN content of the CN/BOB heterojunctions increased, the photocatalytic efficiency increased to the maximum and then decreased due to CN redundancy (Fig. S9†). CN/BOB-16 exhibits the best photocatalytic performance among the catalysts studied in this work, presenting nearly 100% degradation efficiency within 105 min (Fig. 5a). Thus, CN/BOB-16 was adopted to degrade BPA (Fig. 5d). Photocatalytic degradation of BPA was conducted, achieving 98% efficiency within 80 min. Fig. 5b and e show the UV-vis spectra of RhB and BPA degradation over time, with RhB almost always converted to CO_2 and H_2O. In Fig. S16,† we tested the degradation properties of CN/BOB-16 for three other dyes:

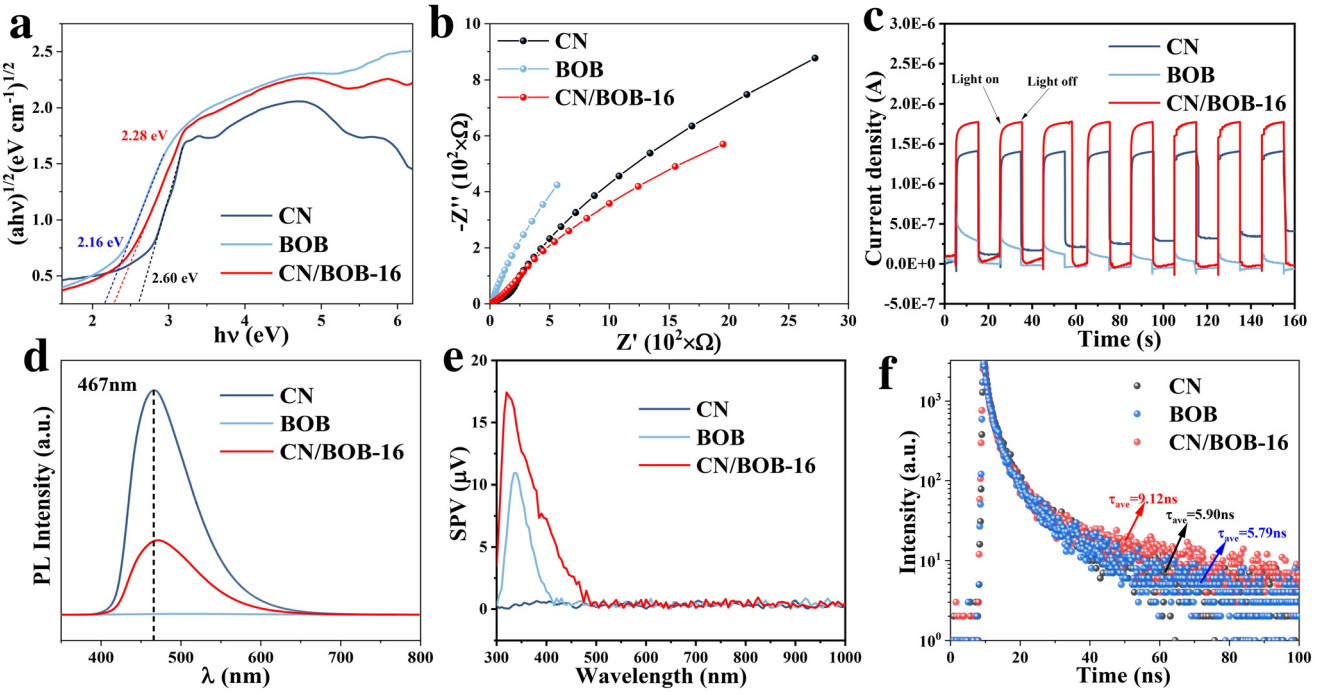

Fig. 6 (a) $(\alpha h\nu)^{1/2}$–$h\nu$ UV-vis DRS spectra; (b) EIS measurement results; (c) transient photocurrent response; (d) photoluminescence spectra; (e) SPV spectrum; (f) PL decay curves of g-C_3N_4/$Bi_4O_5Br_2$-16 and g-C_3N_4.

methyl blue at 90%, methyl orange at 71%, and methyl violet at 75%. The catalyst is suitable for a broader range of applications.

Additionally, kinetic curves and correlation coefficients (r^2) were presented in Fig. S9b–d and Tables S1 and S2† to analyze the photocatalytic process of BPA and RhB. All catalysts were observed to conform to the pseudo-first-order kinetic model, as shown in Fig. S9c and d.† As anticipated, CN/BOB-16 exhibits the highest rate constant (k) value of 0.1 min^{-1}, surpassing the other catalysts investigated in this study (Table S1†). The CN/BOB-16 exhibited the highest photocatalytic degradation efficiency and recorded the lowest time among the recently reported literature (Fig. S10 and Table S4†).

Moreover, the long-term stability of the catalyst is a crucial consideration for practical applications. To investigate the stability of the CN/BOB-16, a recycling photocatalytic degradation RhB test was performed for five cycles and demonstrated excellent stability without significantly reducing the photocatalytic efficiency (Fig. S11a†). The photographs of the dye solvent for the degradation experiment of the fifth cycle were illustrated along with the reaction time (Fig. S12a†), confirming that CN/BOB-16 indeed has superior photocatalytic efficiency and durability. SEM was initially conducted before and after the degradation test to understand the underlying reasons, revealing minimal changes in the morphology of the CN/BOB-16 surface (Fig. S12b†). Also, its crystal structure was characterized *via* XRD profiles (Fig. S11b†), asserting the retention of the crystal structure, consistent with the SEM images. The result above depicts CN/BOB-16 as a suitable catalyst for applying dye degradation.

2.3 The photocatalytic degradation mechanism investigations

Radical trapping experiments were conducted on CN/BOB-16 to investigate the involvement of reactive active species during photocatalytic degradation (Fig. 5c and f). Potassium iodide (KI) and isopropanol (IPA) were used to scavenge the three most active intermediate radicals, h^+ and ·OH, respectively, while nitrogen (N_2) excluded oxygen from the system and inhibited the formation of $\cdot O_2^-$. The degradation rate of RhB decreased to 28.1% and 50% upon introducing the scavengers N_2 and KI, respectively, suggesting that $\cdot O_2^-$ and h^+ are the dominant active species during photocatalytic reactions. The trend of the degradation rate of BPA under different inhibitors was similar to that of RhB. Simultaneously, we used EPR spectroscopy to detect the radicals $\cdot O_2^-$ and ·OH. As shown in Fig. 5g–l, no significant radical signals were observed under dark conditions, but corresponding peaks appeared after 15 min of light exposure, indicating the generation of $\cdot O_2^-$ and ·OH radicals during the photocatalytic process. It can be observed that all samples exhibited characteristic peaks of $\cdot O_2^-$ and ·OH radicals, with CN/BOB-16 showing the most vigorous intensity. This indicates that forming a Z-scheme heterostructure leads to more efficient generation of $\cdot O_2^-$ and ·OH radicals. For the $\cdot O_2^-$ radicals, the intensity of CN was significantly more robust than that of BOB, which is consistent with the characteristics of Z-scheme photocatalysts. The degradation products of bisphenol A (BPA) were investigated using high-performance liquid chromatography-mass spectrometry (HPLC-MS). The seven product ions detected were m/z 243, m/z 241, m/z 275, m/z 183, m/z 133, m/z 149, and m/z 151, as shown in Fig. S14 and S15.† Two possible degradation pathways of BPA were proposed and demonstrated (additional information was added in the ESI† figure note). In the later stages of the reaction, the above products undergo ring-opening reactions under sustained attack by free radicals to generate small molecule products, which are eventually converted to CO_2 and H_2O. The total organic carbon (TOC) content was directly tested by combustion oxidation-non-dispersive infrared absorption, and the TOC removal rates of CN/BOB-16 were 78.8% and 92.7% for BPA and RhB, respectively (Table S3†).

Additionally, to assess the bandgap of CN, BOB, and CN/BOB-16, UV-vis diffuse reflectance spectroscopy (DRS) was employed, utilizing the Kubelka–Munk formula (Fig. S7 and 6a, eqn (S1)†), indicating that CN, BOB, and CN/BOB-16 displayed a bandgap value of 2.60, 2.16, and 2.28 eV, respectively. Electrochemical impedance spectroscopy (EIS) was also tested, as shown in Fig. 6b. CN/BOB-16 has the smallest semicircular arc radius, which confirms that the heterostructure formed promotes the migration of photogenerated carriers. Furthermore, the photocurrent response spectra were measured, indicating the photocatalytic carrier transfer processes. As expected, The photocurrent response of the CN/BOB-16 was more remarkable than that of CN and BOB, respectively (Fig. 6c). Pure CN exhibited a prominent emission peak centered at 467 nm, indicating significant charge recombination (Fig. 6d). Upon addition of BOB to CN, the emission intensity decreased due to the formation of a heterojunction between CN and BOB. The photoelectric effects of the three catalysts in the samples were explored using locked-base surface photovoltage (SPV) measurements (Fig. 6e). The SPV response of CN/BOB-16 was significantly more robust than that of CN and BOB, probably due to the interfacial interactions between CN and BOB. BOB showed a pronounced response to light irradiation in the range of 300–410 nm, which was attributed to the interband charge of the BOB jump induced. In contrast, the intensity of the SPV response of CN/BOB-16 is much stronger than that of BOB, and the response region can be significantly extended to visible light. This suggests that the composition of CN/BOB-16 heterojunction enhances the photogenerated charge-carrier separation efficiency compared with CN and BOB.

The lifetime of electron–hole pairs' carriers is assessed through photoluminescence (PL) (Fig. 6f). Consequently, CN-BOB-16 exhibits a longer lifetime than CN, indicating a lower recombination rate of electron–hole pairs and, higher photocatalytic activity. Finally, we proposed the reaction pathway to elucidate the degradation mechanism (Fig. S13 and eqn (S7)–(S12)†). Thus, from Fig. S6 and S7,† the CB values of CN and BOB can be calculated to be −1.06 eV and −0.13 eV, respectively, while the corresponding VB values are 1.54 eV and 2.03 eV, respectively.

The dominant active species, h^+ and $\cdot O_2^-$, identified through the free radical capture experiment, are generated at the CB of CN and the VB of BOB. Standard redox potential $O^2/\cdot O_2^-$ about −0.33 eV is higher than the CB of CN, depicting that the electron can reduce the O_2 to $\cdot O_2^-$ (eqn (S9)†). Furthermore, the holes located at the valence band (VB) of BOB possess a more positive potential for oxidizing OH^- to form ·OH (eqn (S10)†). As a result, h^+ and $\cdot O_2^-$ could be generated from this heterostructure system to decompose RhB molecules into smaller intermediates or final products such as CO_2 and H_2O (eqn (S11) and (S12)†). Based on the preceding discussion, the CN/BOB-16 heterojunction, featuring a Z-scheme band scheme, enhances the separation efficiency of photoinduced carriers and preserves a high redox capacity, thereby enhancing photocatalytic performance. The synergistic effects of CN/BOB-16 are crucial in converting RhB pollutants into non-toxic CO_2 and H_2O *via* the excellent active radicals of h^+ and $\cdot O_2^-$ under visible light conditions.

3 Conclusion

In summary, we fabricated various mass ratio CN/BOB heterostructures utilizing a simple and economical ultrasonic-assisted stir process. The optimized CN/BOB-16 exhibited superior photocatalytic performance compared to the catalyst investigated in this study, showcasing rapid kinetics and outstanding stability. It displayed high degradation efficiency for RhB and BPA under visible light conditions, surpassing recently reported catalytic systems in the literature. Through experimental and theoretical approaches, it is shown that the successful formation of CN/BOB heterojunctions is related to the electrostatic potential field at their interfaces, and that CN/BOB-16 as the optimal ratio allows for optimal photogenerated carrier lifetimes, and hole- and electron-pair compositions with respect to other ratios. Through free radical trapping and ESR experiments, it was confirmed that h^+ and $\cdot O_2^-$ its play the most important role in the photocatalytic reaction, and also because of the composition of the z-type heterojunction of CN/BOB, the enhancement of the light utilization reduces the complexation of photogenerated electrons. Ultimately, it makes the redox action of holes and electrons respectively. This study demonstrated the potential of the CN/BOB-16 heterojunction for environmental remediation applications and offers a promising approach for developing mediated Z-scheme heterojunctions with enhanced photocatalytic performance.

4 Experimental section

4.1 Chemical reagents

Bismuth nitrate pentahydrate ($Bi(NO_3)_3{\cdot}5H_2O$), hexadecyl trimethyl ammonium bromide (CTAB), and sodium hydroxide (NaOH) were purchased from Shanghai Yien Chemical Technology Co., LTD. Melamine and ethylene glycol (EG) were supplied by Tianjin Kemiou Chemical Reagent Co., LTD. All of these materials were analytically pure and utilized directly.

4.2 Preparation of $Bi_4O_5Br_2$

Weigh the drug $Bi(NO_3)_3{\cdot}5H_2O$ (2.9625 g) and CTAB (cetyltrimethylammonium bromide,1.3666 g) respectively, and pour 40 ml of EG into solution A and solution B respectively. Both solutions were put into ultrasonic equipment for 15 min, then solution B was pure into solution A, stirred in an agitator for 30 min, and the pH = 8.5 of mixed solution. Pour the prepared solution into a reactor lined with polytetrafluoroethylene, react at 180 °C by microwave hydrothermal method for 30 min, cool to room temperature, wash the reaction product with deionized water, and absolute ethanol many times, dry and grind to obtain BOB sample.

4.3 Preparation of g-C_3N_4

Pristine CN was synthesized using a simple thermal polycondensation method. In a typical procedure, 30 g of melamine was placed in a covered crucible, then heated in a muffle furnace at 550 °C for 4 hours and allowed to cool to room temperature. Next, the powder underwent a second reaction in a muffle furnace, where it was maintained at 550 °C for three hours and then cooled to room temperature at a ramp rate of 3 °C min^{-1}. Finally, the resulting white samples were ground into powders for further use.

4.4 Preparation of g-C_3N_4/$Bi_4O_5Br_2$

Using a simple ultrasonic agitation method, weigh CN and BOB in 50 ml deionized water according to the mass ratio of 2 : 1, 1 : 1, 1 : 2, 1 : 4, 1 : 6, 1 : 8, 1 : 10, ultrasonic treatment for 2 h, and then stir for 24 h. They are named CN/BOB-21, CN/BOB-11, CN/BOB-12, CN/BOB-14, CN/BOB-16, CN/BOB-18, CN/BOB-110, respectively.

4.5 Characterization parameters

The specimens' microstructure was analyzed using X-ray diffraction (XRD) in the 2θ range of 10–80° with a Cu target (λ, Kα1 = 1.54056 Å) generating X-ray radiation. The instrument operated at 40 kV and 30 mA, scanning at 6° min^{-1} with a step size of 0.02°. Transmission electron microscopy (TEM) was utilized to examine micromorphology and microstructure at an operating voltage of 200 kV. Scanning electron microscopy (SEM) was employed to observe morphology with a 3.0 kV beam voltage. Elemental mapping was conducted using energy-dispersive X-ray spectroscopy (EDS). The samples were measured by *in situ* irradiated X-ray photoelectron spectroscopy (ISIXPS) using an Al Kα source to characterize the element types, chemical valence states, chemical bonds, and other electronic structure information. The relevant energy spectra of the samples before and after illumination were detected by using a xenon lamp (500 W) under normal temperature and pressure. The visible light response range of the sample was tested by ultraviolet-visible diffuse reflectance spectroscopy (UV-vis DRS), and the band gap value of the sample can be obtained according to the formula $(\alpha h\nu = A(h\nu - E_g)^{1/2})$. Photoluminescence (PL) was used to analyze the recombination rate of photogenerated electron–hole pairs.

The time-resolved fluorescence data for samples were measured using the Edinburgh FLS1000. The electrochemical workstation studied the electrochemical impedance spectrum, transient photocurrent and Mott–Schottky experiment of the samples. Electron paramagnetic resonance (EPR) was used to verify the production of free radicals. The high-performance liquid chromatography-mass spectrometry (HPLC-MS) method was used to detect the intermediates of photocatalytic degradation and analyze the degradation pathway of pollutants. Total organic carbon was tested by a Vario-TOC instrument of German ELEMENTAL.

4.6 Photocatalytic degradation experiment

BPA and RhB were selected as the target pollutants to assess photocatalytic activity. Specifically, 50 mg of catalyst was added to a 10 mg L^{-1} BPA or RhB solution, and the mixtures were stirred in darkness for 30 min to reach adsorption–desorption equilibrium. A 500 W xenon lamp served as the light source for the photodegradation of the RhB solution (Fig. S1†). The degradation reaction took place under stirring conditions at various time points. At each interval, 5 ml of solid particles were extracted for centrifugation to precipitate, and the respective supernatants were collected. The absorbance (ABS) values were measured using a UV spectrophotometer, with absorption wavelengths ranging from 190 to 400 nm (450 nm to 600 nm). The residual degradation ratio of BPA or RhB was calculated as $\eta = C/C_0$, where C_0 (mg L^{-1}) and C (mg L^{-1}) represent the initial concentration of the dye and the mass concentration of the dye solution at time t, respectively.

4.7 Reactive species capture experiment

Various radical scavengers were employed to investigate their impact on the degradation of RhB, aiming to elucidate the underlying photodegradation mechanism. A 500 W xenon gas lamp with a 400 nm cut-off filter to eliminate UV light served as the light source. In a typical photocatalysis experiment, 50 mg of photocatalyst powder was dispersed into a 50 mL RhB aqueous solution (10 ppm). Potassium iodide (KI), isopropanol (IPA), and nitrogen (N_2) were used as scavengers for energetically oxidizing valence band maximum (VBM)-generated holes (h^+), hydroxide radicals ($\cdot OH^-$), and superoxide radicals ($\cdot O_2^-$), respectively. The presence and roles of various active species were validated by assessing the intensity of photodegradation.

4.8 Computational details

All theoretical investigations were performed *via* the DS-PAW code[45] integrated with the Device Studio program.[46] To investigate the interface charge transfer, the work function of the surface was conducted using the Perdew–Burke–Ernzerhof (PBE) exchange–correlation function and the Hartree–Fock method to get a highly accurate interatomic potential. The cutoff energy and k-point were set to 400 eV, and 5 × 3 × 1, and the optimal geometry was collected based on the electron-step energy convergence criterion of 10^{-4} eV. Moreover, to avoid the interaction between layers, the vacuum thickness was set to 20 Å, and the method of dipole correction was adopted.[45]

Data availability

The data that support the findings of this study are available from the corresponding authors, upon reasonable request.

Conflicts of interest

There are no conflicts to declare.

Acknowledgements

This research was funded by the National Natural Science Foundation of China (Grant No. 22175059 and No. 62264015). This research was supported by the Scientific and Technological Innovation Team (2017CXTD-01) and the 2021 Innovation and Entrepreneurship for Undergraduates (202110719019). We gratefully acknowledge HZWTECH for providing computation facilities.

References

1 G. Crini and E. Lichtfouse, Advantages and disadvantages of techniques used for wastewater treatment, *Environ. Chem. Lett.*, 2019, **17**, 145–155.
2 S. M. Korotta-Gamage and A. Sathasivan, A review: Potential and challenges of biologically activated carbon to remove natural organic matter in drinking water purification process, *Chemosphere*, 2017, **167**, 120–138.
3 S. Wacławek, D. Silvestri, P. Hrabák, V. V. T. Padil, R. Torres-Mendieta, M. Wacławek, M. Černík and D. D. Dionysiou, Chemical oxidation and reduction of hexachlorocyclohexanes: A review, *Water Res.*, 2019, **162**, 302–319.
4 S. H. S. Chan, T. Yeong Wu, J. C. Juan and C. Y. Teh, Recent developments of metal oxide semiconductors as photocatalysts in advanced oxidation processes (AOPs) for treatment of dye waste-water, *J. Chem. Technol. Biotechnol.*, 2011, **86**, 1130–1158.
5 S. H. Lin and C. F. Peng, Treatment of textile wastewater by electrochemical method, *Water Res.*, 1994, **28**, 277–282.
6 L. Jian, G. Wang, X. Liu and H. Ma, Unveiling an S-scheme F–Co_3O_4@Bi_2WO_6 heterojunction for robust water purification, *eScience*, 2024, **4**, 100206.
7 P. V. L. Reddy and K.-H. Kim, A review of photochemical approaches for the treatment of a wide range of pesticides, *J. Hazard. Mater.*, 2015, **285**, 325–335.
8 A. Fujishima and K. Honda, Electrochemical photolysis of water at a semiconductor electrode, *Nature*, 1972, **238**, 37–38.
9 Y. Cong, Y. Ge, T. Zhang, Q. Wang, M. Shao and Y. Zhang, Fabrication of Z-scheme Fe_2O_3–MoS_2–Cu_2O ternary nanofilm with significantly enhanced photoelectrocatalytic performance, *Ind. Eng. Chem. Res.*, 2018, **57**, 881–890.
10 L. Li, S. Xiao, R. Li, Y. Cao, Y. Chen, Z. Li, G. Li and H. Li, Nanotube array-like WO_3 photoanode with dual-layer oxygen-evolution cocatalysts for photoelectrocatalytic overall water splitting, *ACS Appl. Energy Mater.*, 2018, **1**, 6871–6880.

11 Y. Sun, B. Xu, Q. Shen, L. Hang, D. Men, T. Zhang, H. Li, C. Li and Y. Li, Rapid and efficient self-assembly of Au@ ZnO core–shell nanoparticle arrays with an enhanced and tunable plasmonic absorption for photoelectrochemical hydrogen generation, *ACS Appl. Mater. Interfaces*, 2017, **9**, 31897–31906.

12 L. Ge, B. B. Shao, Q. H. Liang, D. L. Huang, Z. F. Liu, Q. Y. He, T. Wu, S. H. Luo, Y. Pan, C. H. Zhao, J. H. Huang and Y. M. Hu, Layered double hydroxide based materials applied in persulfate based advanced oxidation processes: Property, mechanism, application and perspectives, *J. Hazard. Mater.*, 2022, **424**, 127612.

13 X. C. Wang, K. Maeda, A. Thomas, K. Takanabe, G. Xin, J. M. Carlsson, K. Domen and M. Antonietti, A metal-free polymeric photocatalyst for hydrogen production from water under visible light, *Nat. Mater.*, 2009, **8**, 76–80.

14 W. Quan, J. Bao, X. Meng, Y. Ning, Y. Cui, X. Hu, S. Yu and H. Tian, 2D/2D Z-scheme photocatalyst of g-C_3N_4 and plasmonic Bi metal deposited Bi_2WO_6: Enhanced separation and migration of photoinduced charges, *J. Alloys Compd.*, 2023, **946**, 169396.

15 J. Bao, X. Jiang, L. Huang, W. Quan, C. Zhang, Y. Wang, H. Wang, Y. Zeng, W. Zhang, Y. Ma, S. Yu, X. Hu and H. Tian, Molybdenum disulfide loading on a Z-scheme graphitic carbon nitride and lanthanum nickelate heterojunction for enhanced photocatalysis: Interfacial charge transfer and mechanistic insights, *J. Colloid Interface Sci.*, 2022, **611**, 684–694.

16 Y. Liu, Y. Yang, B. Zhang, D. Deng, J. Ning, G. Liu, S. Xue, F. Zhang, X. Liu and W. Zhang, Electronic structure and optical properties of CdS/BiOI heterojunction improved by oxygen vacancies, *J. Alloys Compd.*, 2023, **955**, 170235.

17 X. S. Zhang, Y. Pan, Y. Z. Wang, T. Wu, B. B. Shao, Q. Y. He, L. F. Zhou, T. Li, S. Liu, X. Y. Huang and Z. F. Liu, MOF derived $MnFeO_X$ supported on carbon cloth as electrochemical anode for peroxymonosulfate electro-activation and persistent organic pollutants degradation, *Chem. Eng. J.*, 2024, **481**, 148646.

18 M. S. Akple, J. X. Low, S. Wageh, A. A. Al-Ghamdi, J. G. Yu and J. Zhang, Enhanced visible light photocatalytic H_2-production of g-C_3N_4/WS_2 composite heterostructures, *Appl. Surf. Sci.*, 2015, **358**, 196–203.

19 W. Zhang, B. P. Jia, Q. Z. Wang and D. Dionysiou, Visible-light sensitization of TiO_2 photocatalysts via wet chemical N-doping for the degradation of dissolved organic compounds in wastewater treatment: A review, *J. Nanopart. Res.*, 2015, **17**, 221.

20 Q. M. Sun, W. Ye, J. L. Wei, L. X. Li, J. Wang, J. H. He and J. M. Lu, Lead-free perovskite $Cs_3Bi_2Br_9$ heterojunctions for highly efficient and selective photocatalysis under mild conditions, *J. Alloys Compd.*, 2022, **893**, 162326.

21 H. Tian, M. Liu and W. Zheng, Constructing 2D graphitic carbon nitride nanosheets/layered MoS_2/graphene ternary nanojunction with enhanced photocatalytic activity, *Appl. Catal., B*, 2018, **225**, 468–476.

22 R. A. He, S. W. Cao, P. Zhou and J. G. Yu, Recent advances in visible light Bi-based photocatalysts, *Chin. J. Catal.*, 2014, **35**, 989–1007.

23 J. Li, G. Zhan and Y. Yu, *et al.*, Superior visible light hydrogen evolution of Janus bilayer junctions via atomic-level charge flow steering[J], *Nat. Commun.*, 2016, **7**(1), 11480.

24 H. F. Cheng, B. B. Huang and Y. Dai, Engineering BiOX (X = Cl, Br, I) nanostructures for highly efficient photocatalytic applications, *Nanoscale*, 2014, **6**, 2009–2026.

25 J. Di, J. X. Xia, M. X. Ji, B. Wang, S. Yin, Q. Zhang, Z. G. Chen and H. M. Li, Advanced photocatalytic performance of graphene-like BN modified BiOBr flower-like materials for the removal of pollutants and mechanism insight, *Appl. Catal., B*, 2016, **183**, 254–262.

26 G. P. Liu, L. Wang, B. Wang, X. W. Zhu, J. M. Yang, P. J. Liu, W. S. Zhu, Z. R. Chen and J. X. Xia, Synchronous activation of Ag nanoparticles and BiOBr for boosting solar-driven CO_2 reduction, *Chin. Chem. Lett.*, 2023, **34**, 107962.

27 R. Q. Li, Y. J. Bian, C. M. Yang, L. Guo, T. X. Ma, C. T. Wang, F. Fu and D. J. Wang, Electronic structure regulation and built-in electric field synergistically strengthen photocatalytic nitrogen fixation performance on Ti-BiOBr/TiO_2 heterostructure, *Rare Met.*, 2024, **43**, 1125–1138.

28 F. Chang, B. Lei, C. Yang, J. Y. Wang and X. F. Hu, Ultra-stable $Bi_4O_5Br_2$/Bi_2S_3 n-p heterojunctions induced simultaneous generation of radicals center dot radical ·OH and center $\cdot O_2^-$ and NO conversion to nitrate/nitrite species with high selectivity under visible light, *Chem. Eng. J.*, 2021, **413**, 127443.

29 F. Chang, C. Yang, J. Y. Wang, B. Lei, S. J. Li and H. Kim, Enhanced photocatalytic conversion of NOx with satisfactory selectivity of 3D-2D Bi4O5Br2-GO hierarchical structures via a facile, *Sep. Purif. Technol.*, 2021, **266**, 118237.

30 Z. H. Wu, J. Shen, N. Ma, Z. F. Li, M. Wu, D. F. Xu, S. Y. Zhang, W. H. Feng and Y. F. Zhu, $Bi_4O_5Br_2$ nanosheets with vertical aligned facets for efficient visible-light-driven photodegradation of BPA, *Appl. Catal., B*, 2021, **286**, 119937.

31 H. Sheng, X. Zhang, S. Xin, H. Shi, G. Liu, Q. Wu, S. Xue, X. Wang, T. Shao, Y. Liu, F. Zhang and X. Liu, First-principles study of electronic structure and optical properties of Ni-doped $Bi_4O_5Br_2$, *Coatings*, 2024, **14**, 67.

32 J. Bao, W. Quan, Y. Ning, H. Wang, Q. Wei, L. Huang, W. Zhang, Y. Ma, X. Hu and H. Tian, Efficient visible-light-driven tetracycline degradation and Cr(VI) reduction over a $LaNi_{1-x}Fe_xO_3$ ($0 \leq x \leq 1$)/g-C_3N_4 type-II heterojunction photocatalyst, *Inorg. Chem.*, 2023, **62**, 1086–1094.

33 Y. Y. Zhou, J. X. Zhang and D. F. Wu, Fabrication of g-C_3N_4/$Bi_4O_5Br_2$ 2D nanosheet photocatalyst for removal of organic pollutants under visible light irradiation, *ChemistrySelect*, 2023, **8**, e202301237.

34 F. T. Yi, J. Q. Ma, C. W. Lin, L. Y. Wang, H. N. Zhang, Y. X. Qian and K. F. Zhang, Insights into the enhanced adsorption/photocatalysis mechanism of a $Bi_4O_5Br_2$/g-C_3N_4 nanosheet, *J. Alloys Compd.*, 2020, **821**, 153557.

35 X. S. Zhao, Y. Y. You, S. B. Huang, Y. X. Wu, Y. Y. Ma, G. Zhang and Z. H. Zhang, Z-scheme photocatalytic production of hydrogen peroxide over $Bi_4O_5Br_2$/g-C_3N_4 heterostructure under visible light, *Appl. Catal., B*, 2020, **278**, 119251.

36 C. Y. Li, Y. J. Fan, S. T. Gu, Y. X. Xiao, X. Y. Zhao, J. M. Nan and X. Xiao, Microwave-assisted construction of 2D/2D

direct Z-scheme g-C_3N_4/$Bi_4O_5Br_2$ heterojunctions with enhanced molecular oxygen activation for boosting selective photocatalytic conversion of benzyl alcohol, *Appl. Surf. Sci.*, 2023, **636**, 157809.

37 Z. Wu, J. Shen, N. Ma, Z. Li, M. Wu, D. Xu, S. Zhang, W. Feng and Y. Zhu, $Bi_4O_5Br_2$ nanosheets with vertical aligned facets for efficient visible-light-driven photodegradation of BPA, *Appl. Catal., B*, 2021, **286**, 119937.

38 J. Xia, J. Di, S. Yin, H. Li, H. Xu, L. Xu, H. Shu and M. He, Solvothermal synthesis and enhanced visible-light photocatalytic decontamination of bisphenol A (BPA) by g-C_3N_4/BiOBr heterojunctions, *Mater. Sci. Semicond. Process.*, 2014, **24**, 96–103.

39 S. X. Yu, J. Y. Li, Y. H. Zhang, M. Li, F. Dong, T. R. Zhang and H. W. Huang, Local spatial charge separation and proton activation induced by surface hydroxylation promoting photocatalytic hydrogen evolution of polymeric carbon nitride, *Nano Energy*, 2018, **50**, 383–392.

40 R. Li, F. X. Xie, J. X. Liu, Y. W. Wang, Y. F. Wang, X. C. Zhang and C. M. Fan, Synthesis of $Bi_4O_5Br_2$ from reorganization of BiOBr and its excellent visible light photocatalytic activity, *Dalton Trans.*, 2016, **45**, 9182–9186.

41 G. Song, Z. Chu, W. Jin and H. Sun, Enhanced performance of g-C_3N_4/TiO_2 photocatalysts for degradation of organic pollutants under visible light, *Chin. J. Chem. Eng.*, 2015, **23**, 1326–1334.

42 W. Yan, L. Yan and C. Y. Jing, Impact of doped metals on urea-derived g-C_3N_4 for photocatalytic degradation of antibiotics: Structure, photoactivity and degradation mechanisms, *Appl. Catal., B*, 2019, **244**, 475–485.

43 J. Li, X. Y. Wu, W. F. Pan, G. K. Zhang and H. Chen, Vacancy-rich monolayer BiO_{2-x} as a highly efficient UV, visible, and near-infrared responsive photocatalyst, *Angew. Chem., Int. Ed.*, 2018, **57**, 491–495.

44 X. Xiao, C. Liu, R. P. Hu, X. X. Zuo, J. M. Nan, L. S. Li and L. S. Wang, Oxygen-rich bismuth oxyhalides: Generalized one-pot synthesis, band structures and visible-light photocatalytic properties, *J. Mater. Chem.*, 2012, **22**, 22840–22843.

45 P. E. P. Blöchl, Projector augmented-wave method, *Phys. Rev. B: Condens. Matter Mater. Phys.*, 1994, **50**, 17953.

46 D. S. Hongzhiwei Technology, Version 2022A, China, 2021, Available online: **https://iresearch.net.cn/cloudSoftware**.